Low Frequency Quasi-periodic Oscillation in MAXI J1820+070: Revealing distinct Compton and Reflection Contributions

Chenxu Gao[1,2], Zhen Yan[1]⋆, Wenfei Yu[1]†

[1]*Shanghai Astronomical Observatory, Chinese Academy of Sciences, 80 Nandan Road, Shanghai 200030, China*
[2]*University of Chinese Academy of Sciences, 19A Yuquan Road, Beijing 100049, China*

ABSTRACT

X-ray low frequency quasi-periodic oscillations (LFQPOs) of black hole X-ray binaries, especially those type-C LFQPOs, are representative timing signal of black hole low/hard state and intermediate state, which has been suspected as to originate due to Lense-Thirring precession of the accretion flow. Here we report an analysis of one of the *Insight*-HXMT observations of the black hole transient MAXI J1820+070 taken near the flux peak of its hard spectral state during which strong type-C LFQPOs were detected in all three instruments up to photon energies above 150 keV. We obtained and analyzed the short-timescale X-ray spectra corresponding to high- and low-intensity phases of the observed LFQPO waveform with a spectral model composed of Comptonization and disk reflection components. We found that the normalization of the spectral model is the primary parameter that varied between the low and high-intensity phases. The variation in the LFQPO flux at the hard X-ray band ($\gtrsim$ 100 keV) is from the Compton component alone, while the energy dependent variation in the LFQPO flux at lower energies ($\lesssim$ 30 keV) is mainly caused by the reflection component with a large reflection fraction in response to the incident Compton component. The observed X-ray LFQPOs thus should be understood as manifesting the original timing signals or beats in the hard Compton component, which gives rise to additional variability in softer energies due to disk reflection.

Key words: accretion, accretion discs – stars: black holes – X-rays: binaries – X-rays: individual: MAXI J1820+070

1 INTRODUCTION

Most of black hole X-ray binaries (BH XRBs) in our galaxy are transient sources. They occasionally experienced an outburst and spent most of their time in quiescence. During an outburst, the X-ray spectral and timing properties usually changes dramatically on a timescale of days to months (Miyamoto et al. 1995; Remillard & McClintock 2006; Done et al. 2007; Belloni & Motta 2016). So different spectral states are classified based on the X-ray spectral and timing properties. The two main spectral states are hard and soft states. The accretion flow in the soft state is thought to be the geometrically thin disk (Shakura & Sunyaev 1973), which is characterised by the multi-temperature black body X-ray spectrum and very low level short term X-ray variability. The X-ray spectra of the hard state are dominated by the inverse Comptonization scattering of the hot corona. A part of the hard X-ray illuminates the accretion disk and then produces a reflection component, which is characterised by the fluorescent iron Kα line and the reflection hump at $\sim$ 30 keV (e.g. Fabian & Ross 2010, , for a review). During the hard state, the X-ray variability amplitude is very high, and low-frequency quasi-periodic oscillations (LFQPOs) are usually detected.

One of the most common type low-frequency QPO for BH XRBs is called type-C QPO, the central frequency of which may evolve in the tens of mHz to 30 Hz range, depending on its spectral state(Psaltis et al. 1999; Casella et al. 2004; Van der Klis 2006). The type-C

QPO generally appears as very strong and narrow peaks in the power spectrum. The origin of type-C QPO is still under debate, and a popular model is the Lense-Thirring precession of the hot flow(see reviews by Ingram & Motta 2019).

Besides conventional timing and spectral analysis of the QPO properties, phase-resolved timing and spectral analysis can provide timing and spectral information of the QPO at different phases, revealing the origin of QPOs (Yu et al. 2001; Yu & van der Klis 2002). Specifically for the LFQPOs in black hole binaries,Miller & Homan (2004) detected variation of the Fe Kα line with QPO phase which suggests that the QPOs originate in the inner disk. Ingram & van der Klis (2015) observed modulation of the Fe Kα line width and reflection component by reconstructing the GRS 1915+105 energy spectrum at different phases, providing evidence for a geometric origin of the X-ray QPO. Later on, more comprehensive analysis of the LFQPOs has been performed with the observations of H1743-322 (Ingram et al. 2016, 2017). Both the iron line energy and the reflection fraction are found modulated with the QPO phase. This is taken as strong evidence supporting the Lense-Thirring precession model.In recent analysis about QPO phase-resolved spectroscopy, Nathan et al. (2022) detected a significant modulation of the reflection fraction in GRS 1915+105, which indicates that the inner accretion disk geometry changes with QPO phase.

MAXI J1820+070 is one of the brightest transient black hole X-ray binaries, which is discovered in X-ray on 2018 March 11 by Monitor of All-sky X-ray Image (MAXI; Kawamuro et al. 2018; Tucker et al. 2018). The X-ray intensity of the source increased rapidly and

---

⋆ zyan@shao.ac.cn for correspondence on spectral analysis
† wenfei@shao.ac.cn for correspondence on timing analysis

reached a peak of 2 Crab at 2-20keV around March 20 (Shidatsu et al. 2018), and then the source stayed in the hard state for roughly three months with slowly decreasing luminosity (Shidatsu et al. 2019). This unusually long and bright hard state makes it an excellent target to study the rich soft and hard X-ray spectral and timing phenomena (e.g. Kara et al. 2019; Ma et al. 2020; Stiele & Kong 2020; You et al. 2021). As optical LFQPOs are observed at frequencies nearly identical to that seen in the X-ray band (Yu et al. 2018b,a), multi-wavelength timing observations of the LFQPOs will provide critical clues to the origin of the LFQPOs as well (Mao et al. 2022).

Insight-Hard X-ray Modulation Telescope (HXMT) consists of three payloads: high energy X-ray telescope (HE, 20–250 keV), medium energy X-ray telescope (ME, 5–30 keV), and low energy X-ray telescope (LE, 1–15 keV)(Zhang et al. 2020). The technical details of *Insight*-HXMT can be seen in data reduction guide[1]. *Insight*-HXMT has performed high cadence monitoring observations for this outburst. The broad X-ray energy band and the high count rate during the hard state observations provide us an opportunity to explore the energy spectrum evolution on short timescale. In this work, we use the *Insight*-HXMT data to explore the broadband X-ray spectral variation within the LFQPO timescale.

2 DATA ANALYSIS AND RESULTS

2.1 Data reduction

We used the observation taken on March 27, 2018 (ObsId P0114661006), when the flux is near its maximum of the hard state (Shidatsu et al. 2019). The exposure time of this observation is about 3400s.

We used the *Insight*-HXMT data analysis software HXMTDAS v2.05 to extract the data from three payloads. To avoid contamination from nearby sources, we chose the narrow FOVs for all three telescopes. For creating good-time-intervals (GTIs), we used the suggested criteria in the guide. We then generated the energy spectrum and the corresponding background from the screened event, as well as the light curve of 8ms resolution.

2.2 Spectral analysis

We grouped the spectra with minimum of 20 counts per bin. The spectral fitting performed by XSPEC version 12.11.1 with Chi statistics. We apply this model constant×TBabs×(diskbb+reflkerr) to fit the spectra with energy bands 2–8keV for LE, 10–30keV for ME, 35–150keV for HE. The constant factor is used to account for differences of flux calibration between different payloads. The TBabs accounts for interstellar absorption, with N_H fixed at $1.5 \times 10^{21} cm^{-2}$(Uttley et al. 2018), where abundances and cross sections of the absorption by the Galactic interstellar medium are set according to Wilms et al. (2000) and Verner et al. (1996). The diskbb is a multiple blackbody component. The reflkerr is a relativistic reflection model which includes a thermal Comptonization continuum as the illuminating source (compps), which is one of the most accurate models of this process, and a hybrid model of rest-frame reflection hreflect (Niedzwiecki et al. 2019). The ionization parameter of the disk $\log \xi$ is defined as the same way as the xillver (Garcia & Kallman 2010), $\xi = 4\pi F_{irr}/n_e$, where the F_{irr} is the irradiating flux in the 13.6 eV-13.6 keV photon energy range and n_e is fixed as $10^{15} cm^{-3}$, **and without taking into account the ionization gradient.** The comparison

[1] http://hxmten.ihep.ac.cn/SoftDoc/501.jhtml

between the reflkerr and the other popular relativistic reflection model relxill is extensively shown in Dziełak et al. (2019).

During the spectral fitting, we fixed the black hole spin at 0.13 (Zhao et al. 2021) and the inclination angle at 63° (Atri et al. 2020). The disk temperature is set as the seed photon temperature for Comptonization. The normalization of the diskbb component N_{disk} is expressed as $(R_{in}/D_{10})^2 \cos\theta$, where R_{in} is the inner disk radius in km, D_{10} is the distance to the source in units of 10 kpc and θ is inclination angle. We obtained $N_{disk} \simeq 816(R_{in}/R_g)^2$ by taking the distance as 2.96 kpc (Atri et al. 2020), the black hole mass as $8.48M_\odot$ (Torres et al. 2020), and the inclination angle as 63° (Atri et al. 2020). Then N_{disk} is tied to the parameter R_{in} (in unit of R_g) in reflkerr as $816R_{in}^2$. The best-fitting parameters are shown in the first row of Table 1. The reduced chi-square value indicates that our model is adequate to describe the data. We also noticed that some spectral fittings need an additional unchanged non-relativistic reflection component during the hard state (Buisson et al. 2019; You et al. 2021). However, whether including the non-relativistic reflection component does not affect the estimation of the relativistic reflection component and the Comptonization component (You et al. 2021).

2.3 Timing analysis

We generated the power density spectra(PDS) of different energy bands by using powspec with frequency resolution $d\nu = 1/512$ Hz and Nyquist frequency $\nu_N = 256$Hz. We then calculated the rms normalized power by dividing the mean count rate for different energy bands respectively(van der Klis 1995, and references therein) and subtracted the white noise. We rebined the PDS with a geometric index of 1.08 and fitted the broadband noise with three Lorentzians and the QPO and its harmonic frequencies with three narrow Lorentzians in XSPEC v12.11.1. The best-fitted reduced χ^2 are all less than 1.0. The PDS data and the best-fitting model are plotted in Figure 1. The LFQPO around 0.044 Hz is clearly detected as indicated by the curves in black in different energy bands. We show the best-fitting LFQPO results in Table 2. The central frequency of the LFQPO is constant with the same in different energy bands. The RMS of the LFQPO however decreases with photon energy in the energy range above ~10 keV, which is different from other black hole transients (e.g. Huang et al. 2018).

Figure 2 shows the light curves of three instruments with time resolution of 5 seconds. There are visible flares on the timescales similar to that of the detected LFQPO. In order to quantitatively identify the peak (high intensity) and trough (low intensity) phases of the flares corresponding to the LFQPO waveform, we used the local maxima/minima method to select the extreme from the beginning to the end of the light curve. The method takes a fixed-width window and moves in order from the light curve without overlapping, picking the extreme values of the curve in the window with each move. Since the central frequency of the detected QPO is 0.044 Hz with an FWHM is 0.013 Hz (roughly corresponding to a timescale 20-30 seconds), we then set the window width as 25 s in order to match the QPO cycles. We set the minimum intensity F_{min} and the maximum intensity F_{max} of the light curve as two reference flux baselines and their intensity difference is ΔF. In order to ignore the flares with small fluctuations, we exclude peaks below $F_{max} - 0.7\Delta F$, and troughs above $F_{min} + 0.18\Delta F$. Under the above conditions, we selected 113 peaks and 118 troughs, which 113 pairs of peak and trough phases are adjacent. The selection of the peak phases and the trough phases was only performed in the LE light curve, which is shown in Figure 2.
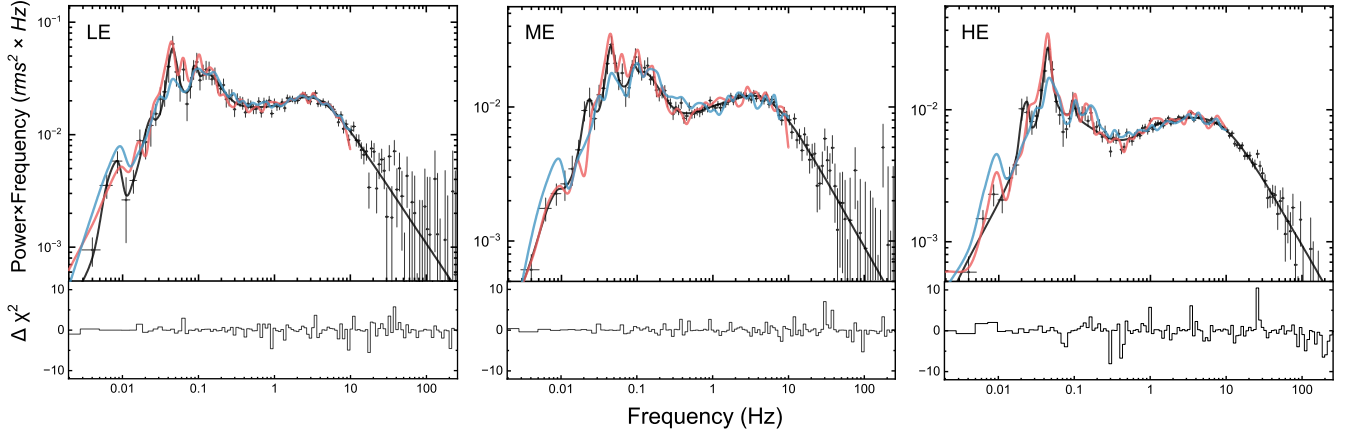
Figure 1. Upper: PDSs of LE, ME and HE light curves and faked light curves. The PDS of the original X-ray light curve is shown as black dots and the best-fitting model is shown as black solid line. The PDSs of identified flares (occupy ~ 40% of the entire exposure) is shown in red, and the PDS of non-flare intervals is shown in blue (for clarity, the uncertainties and the PDS above 10Hz are not plotted). By comparing the PDSs corresponding to the flare and non-flare intervals, we show that the power of the LFQPO is well accounted for by those identified flares. Lower: The contribution to the chi-square of each bin.
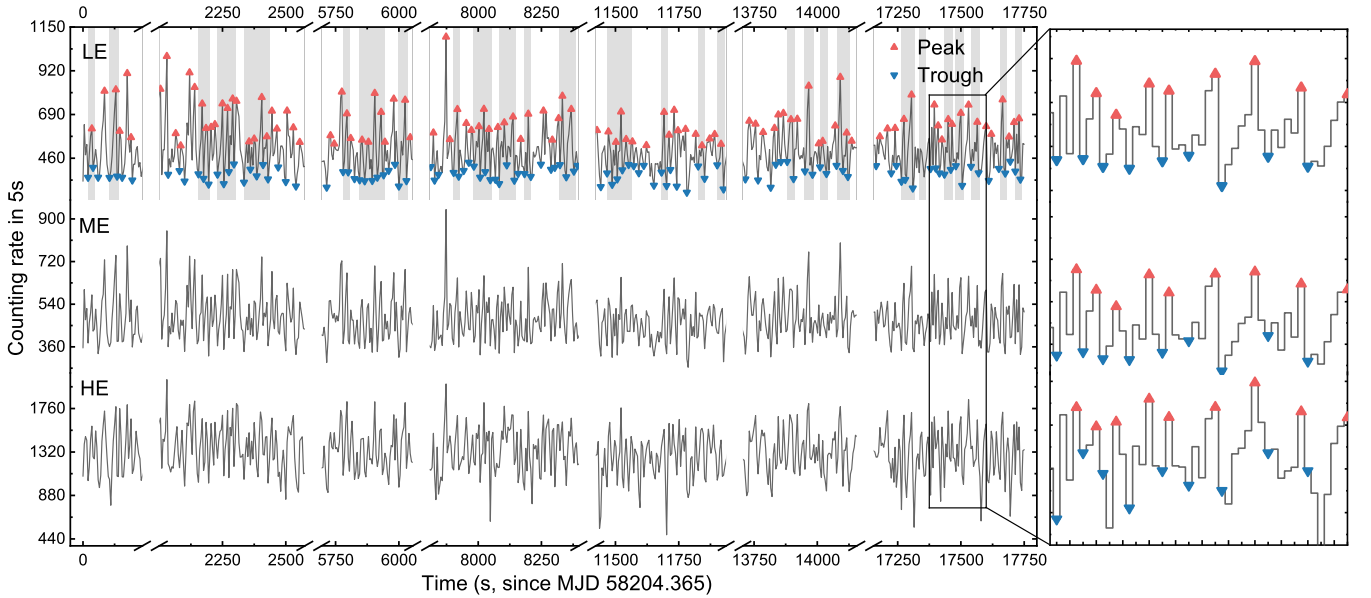

Figure 2. The background-subtracted light curves obtained in the observation `P011466100601` with a time resolution of 5 seconds. LE, ME and HE light curves are shown in the left panel from top to bottom, respectively. The triangle markers in the LE light curves indicate peak (red) and trough (blue) intervals we identified for the LFQPOs, respectively. **The shaded region in LE light curve indicates the interval of identified flares, the PDS of which shows that the QPO mostly account for those identified flares (see Figure 1).** The right panel is a zoom-in on a segment of the light curve.

To check whether the peaks and troughs of the selected flares are consistent with the QPO waveform, we produced a power spectrum of a faked light curve consisting of these selected flares. The interval between two neighbor trough is identified as a full flare, which corresponds to the QPO waveform with the time interval less than or equal 30 s. These identified flares covered ~ 40% of the entire light curve exposure (see the shaded region of Figure 2). We then generate two fake light curves based on the identified flare intervals. One is that the count rates during the flare intervals are retained, while the count rates during the non-flare intervals are replaced by the average count rate specific to each interval. The other is that the count rates during the flare intervals are replaced by their corresponding average count

rate, while non-flare intervals are retained. The PDSs of the above fake light curves are shown in red and blue solid lines in Figure 1. It is obvious that the power spectra of the faked light curve of flare intervals show strong LFQPO. The power at the QPO frequency of 0.044 Hz in the faked PDS of flare intervals is larger than that of the non-flare intervals by a factor of 2.2 for the LE band, 2.0 for the ME band, and 2.0 for the HE band, respectively. At the same time, the band-limited noise components, e.g., the peaked noise in 1–10 Hz, are consistent with the same between that of the flare intervals and that of the non-flare intervals. The observed power of the LFQPO, especially that of the fundamental QPO peak, is mostly accounted for by those identified flares, demonstrating that the peak phase and

Table 1. Spectral parameters of the energy spectra corresponding to the LFQPO peak phase, trough phase and the average. All errors indicate 68% of the uncertainty interval

Parameter	Total	Peak	Trough
T_{in} (keV)	$0.32^{+0.03}_{-0.03}$	$0.32^{+0.12}_{-0.03}$	$0.33^{+0.11}_{-0.02}$
R_{in} (R_g)	$2.58^{+0.34}_{-0.2}$	$2.78^{+0.38}_{-0.76}$	$2.84^{+0.51}_{-0.78}$
A_{Fe}	$3.53^{+0.19}_{-0.35}$	—	—
τ	$4.43^{+0.12}_{-0.17}$	$4.39^{+0.21}_{-0.1}$	$4.59^{+0.22}_{-0.15}$
kT_e (keV)	$44.36^{+1.59}_{-1.08}$	$45.1^{+1.24}_{-2.18}$	$43.6^{+0.96}_{-1.62}$
$\log\xi$	$3.78^{+0.06}_{-0.04}$	—	—
$\mathcal{R}$	$1.18^{+0.07}_{-0.04}$	$1.28^{+0.1}_{-0.1}$	$1.05^{+0.1}_{-0.11}$
$norm$	$1.65^{+0.09}_{-0.11}$	$2.03^{+0.14}_{-0.35}$	$1.0^{+0.09}_{-0.21}$
χ^2/dof	1138/1235	1286/1226	1412/1184

Table 2. Best-fitting results for LFQPO around 0.044 Hz in different energy bands

	ν_{QPO} (Hz)	FWHM	RMS	χ^2/dof
2-8keV(LE)	$0.044^{+0.001}_{-0.002}$	$0.013^{+0.005}_{-0.005}$	$0.156^{+0.026}_{-0.025}$	146/136
10-30keV(ME)	$0.043^{+0.002}_{-0.001}$	$0.014^{+0.005}_{-0.004}$	$0.106^{+0.023}_{-0.018}$	132/136
35-150keV(HE)	$0.044^{+0.001}_{-0.001}$	$0.01^{+0.004}_{-0.003}$	$0.093^{+0.007}_{-0.013}$	159/136
100-150keV(HE)	$0.044^{+0.002}_{-0.001}$	$0.009^{+0.003}_{-0.002}$	$0.08^{+0.007}_{-0.007}$	138/136
150-200keV(HE)	$0.044^{+0.004}_{-0.003}$	$0.007^{+0.006}_{-0.005}$	$0.06^{+0.02}_{-0.01}$	140/136

the trough phase we selected represent those of the QPO waveforms. Thus the differences of the energy spectra corresponding to the peak and the trough phases indeed indicate the spectral variation within the LFQPO cycle.

2.4 Short-timescale energy spectra of the LFQPO: the peak phase vs. the trough phase

Then we performed spectral fits to all the energy spectra on 5 second time scales which were extracted in the time intervals corresponding to the peak phase and the trough phase, respectively. For each energy spectrum, we performed Markov Chain Monte Carlo sampling in XSPEC, with the sampling algorithm from the `emcee` software package (Foreman-Mackey et al. 2013). We fixed the following three parameters: the constant value, the iron abundance A_{Fe}, and the ionization parameter $\log\xi$ to the same as the average energy spectrum. We set 20 walkers with the prior parameters from the average energy spectrum fitting result in subsection 2.2. We used a Gaussian prior with a center as the best-fitting value from the parameters of the averaged energy spectrum and a width as 20%. We set 5,000 walkers and 5,000 burn-in steps. The median value of the posterior samples is taken as the best-fitting value for each free parameter. The 68% interval of reduced chi-square extracted from the median value of posterior chi-squares is 0.93 to 1.1, which indicates that all the 5s energy spectra are well-fitted by the model.

We then obtained the best-fitting parameters for all the X-ray spectra extracted on the 5 second time scale. The histogram of the best-fitting spectral parameters in the peak, trough and other phases are plotted(Figure 3). Then the mean value and 68% interval (16%-84%) for each parameter of each phase are also calculated. We can see that the inner disk radius R_{in}, the electron temperature kT_e and the optical depth τ show almost identical distribution between peak and trough. The other three parameters are larger in the peak phase than

in the trough phase. Especially, the 68% intervals of the normalization $norm$ and the reflection fraction $\mathcal{R}$ show no overlap, indicating a significant difference between these two parameters between peak and trough phases. According to the results, we obtain that the peak and trough phase short timescale spectral parameters T_{in}, $\mathcal{R}$ and $norm$ are different at least 50%, 76% and 96% significance level. So at least the spectral parameter $norm$ significantly changes with the QPO phases . We also generated the respective PDSs for all best-fitting parameters of the short timescale spectra, but only the PDS of the $norm$ shows an apparent QPO feature at the same frequency.

The most significant difference between the energy spectra corresponding to the peak and trough phases is the normalization (see Figure 3). The normalization determines the photon flux of both Compton and reflection components by the same factor. The reflection fraction $\mathcal{R}$ also varies between peak and trough phases. The photon flux of the reflection component is determined by $norm \times \mathcal{R}$ (Niedzwiecki et al. 2019). So the variation of $\mathcal{R}$ makes the flux variability of the reflection component different from that of the Compton component. The normalization and reflection fraction are also found to significantly vary with the QPO phase in another BHXRB H1743−322, in which the normalization is also the parameter that bears the most significant change (Ingram et al. 2017). There is also difference in the inner disk temperature T_{in} between that of the peak and of the trough. Since the disk component was very weak in the observation and the inner disk temperature is tied to the seed photon temperature for Compotonization in the model we applied, we can not distinguish whether the variation in T_{in} was due to intrinsic disk variability or potential variation in the Compton component.

2.5 Averaged energy spectra corresponding to the LFQPO peak and trough phases

In order to compare the energy spectra corresponding to the peak and trough phases in detail with enough statistics, we stacked all the 5-second energy spectra corresponding to either phase. Corresponding response files were generated using the tool `ADDSPEC` and the background file was generated using the tool `MATHPHA`, respectively. We also used the same spectral model that was used to fit the average energy spectrum to fit the stacked energy spectra. We fixed the constant value, the iron abundance A_{Fe} and the ionization parameter $\log\xi$ in the model at the same values obtained in the spectral fit of the average energy spectrum. The best-fitting spectral parameters corresponding to the peak and the trough phases are listed in Table 1. The best-fitting spectral parameters corresponding to the peak and trough phases agree with each other, except for the normalization $norm$, the reflection fraction $\mathcal{R}$. The $norm$ and $\mathcal{R}$ of the peak and trough phases are different by at least 97% and 70% significance levels, which is consistent with the statistical results of the 5-seconds spectra.

We plotted the unfolded energy spectra of peak/trough phases in the top panel of Figure 4. The best-fitting models of the Compton and reflection components are also added in the Figure 4. The spectral shape of the Compton components are almost the same at the peak and the trough phases, since only $norm$ changes and other parameters related to Compton (such as kT_e and τ) remain nearly constant. On the other hand, the spectral shape of the reflection component at the peak phase is different from that at the trough phase, since the reflection fraction $\mathcal{R}$ is larger. The reflection component dominates over the Compton below ~30 keV, and the Compton component becomes dominated above ~70 keV in both peak and trough phases.

The fractional photon flux change in the Compton component between peak and trough phases (C_P-C_T) is almost the same for different energies since the normalization is the only parameter that
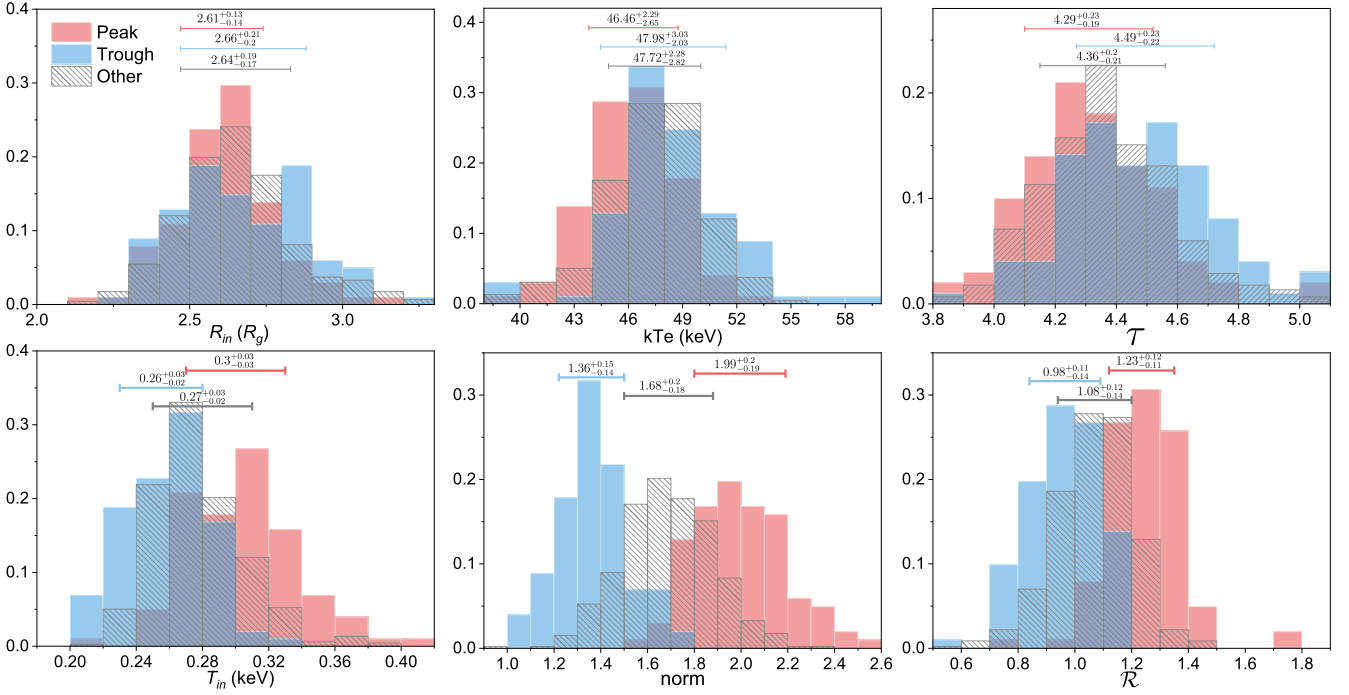
Figure 3. The histogram of the best-fitting parameters of all the X-ray spectra extracted on 5 second time scale. In each graph, the histograms in red represent those spectra during the peak phase, while the histogram in blue represents those spectra during the trough phases, respectively. The histograms of the spectral parameters in neither the peak phase nor the trough phase are shown in shadow. The 68% interval for each parameter in each histogram is marked by a horizontal baa r.

varies. The photon flux variation in the reflection component (R_P-R_T) is roughly two times larger than that of the Compton component below ~10 keV, and becomes less than 1/2 in the energy range above ~100 keV. We then plotted the ratio between the photon flux variation of the reflection and the Compton component between the peak phase and the trough phase, in order to show relative contributions from the Compton and the reflection component to the X-ray variability with photon energy. The QPO fractional RMS below ~10 keV is also larger than that above ~10 keV (see Figure 4), which suggests that strong variation of the QPO flux at lower energy band is due to the reflection component. Since the photon flux variation of the reflection component is determined by the variation of $norm \times \mathcal{R}$, the dominated role of the reflection component below ~10 keV on the QPO flux variation can be understood as the parameter $\mathcal{R}$ of this observation is large.

A remarkable result is shown in Figure 4. Starting from above ~70 keV, the flux variation between the peak phase and the trough phase is becoming primarily from the contribution of the *direct* Compton component. Beyond 100 keV or so, the contribution of the reflection component is negligible. This implies that detection of the LFQPOs at energy above ~100 keV simply means that the Compton component itself produces the LFQPO quasi-periodicity, although the reflection component dominates the LFQPO peak-trough variation below ~30 keV.

3 DISCUSSION

We have investigated the short-timescale X-ray spectra corresponding to the high and low intensity phases of the LFQPO (defined as peak and trough) in one *Insight*-HXMT observation of MAXI

J1820+070. The greatest change among spectral parameters between the two LFQPO phases is the normalization *norm*. The difference in the normalization represents the flux variation between the two phases in the primary Compton emission. In the energy range above ~100 keV, the Compton component overwhelmingly dominates over the reflection component, and thus the flux variation above ~100 between the peak and the trough phases is contributed by the Compton component alone (see Figure 4). Therefore, the underlying beats that generate the LFQPOs should originate from the Compton emission. Under the framework of conventional Comptonization models, the Compton component is thought to originate from a hot corona. Our spectral analysis shows that the corona is not oscillating coronal temperature or electron density, since in our spectral fits, the temperature kT_e and τ of the Compton component does not show apparent changes between those of the peak and the trough phases. Thus the LFQPO corresponds to a modulation in the photon flux of the Compton component, either through modulation of the seed photons or line-of-sight covering factor.

The difference in the reflection fraction $\mathcal{R}$ between the peak and the trough phases demonstrates that the reflection fraction acts like an amplification factor of the variation in the primary incident Compton flux since the photon flux variation in the reflection component is determined by $norm \times \mathcal{R}$. The values of the reflection fraction in the peak and the trough phases are both very large (larger than unity) but different, which causes the flux change between the peak and the trough phases at lower energies (below ~30 keV, see Figure 4) is dominated by the reflection component. The effect of the reflection fraction is also confirmed by that the fractional rms of the LFQPOs at below ~10 keV is higher than that above 10 keV. In conclusion, the modulation in the Compton photons produces the underlying,
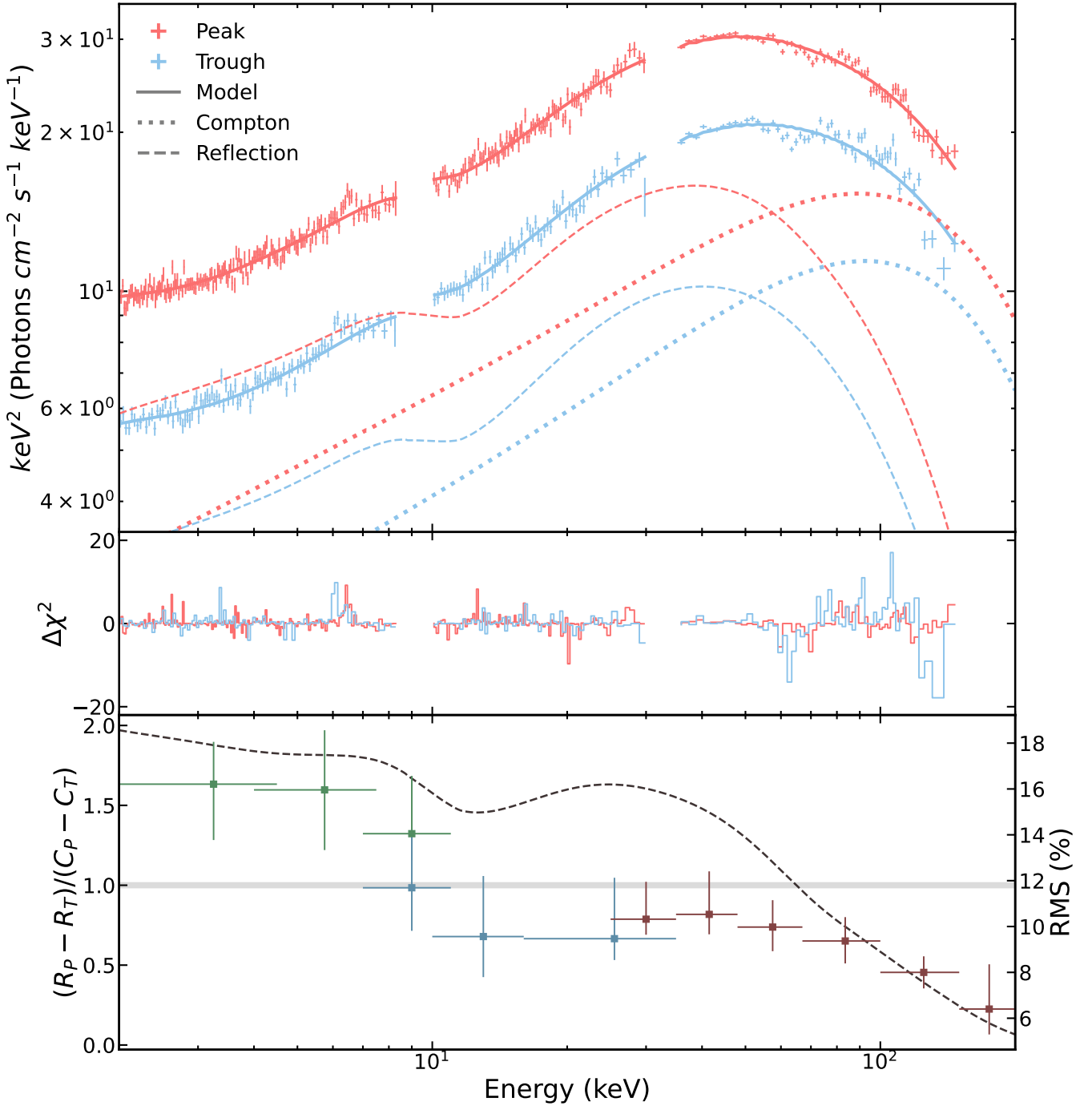
Figure 4. Upper: The unfolded energy spectra corresponding to the peak phase (in red) and the trough phase (in blue) and the corresponding spectral components of the best-fitting models. The solid line shows the total spectrum. The disk component is not shown as it is very weak and negligible. The Compton and reflection components are represented by a dotted line and a dashed line, respectively. Middle: The contributions to the chi-square for the peak and trough spectra. Lower: The ratio between the flux changes between the peak phase and the trough phase in the Compton component and the reflection component (shown as the dashed line), and the QPO fractional RMS vs. energy up to 200 keV (marked in solid square at the lower panel). Here R_P-R_T is the photon flux change of reflection component, and C_P-C_T is the photon flux change of Compton component.

original beats of the LFQPO signal, while the LFQPO amplitude at lower energy bands is primarily contributed by the reprocessed reflection component, which is affected and amplified by the reflection fraction.

Hot accretion flow model has been the popular model to account for the Compton emission in the hard state of BHXRB (Done et al. 2007). In this model, the accretion geometry is composed of a hot accretion flow inside a truncated disk (Esin et al. 1997). The precession of the hot accretion flow can modulate the Compton emission through self-occultation, projected area and relativistic effects, which

produce the observed LFQPO (Ingram et al. 2009). Because there is a misalignment between the hot accretion flow and the accretion disk, the reflection fraction changes with the hot accretion flow precession. The variation of the reflection fraction with LFQPO phases strongly depends on the inclination angle and the truncated disk radius (You et al. 2020).

In an alternative accretion geometry, the so-called lamppost geometry, a point corona lies above the black hole which illuminates the accretion disk. If the precession of the disk is the proposed mechanism to produce the LFQPO under this accretion geometry (Schnittman et al. 2006), the modulation in the Compton component at high energy band (say, e.g., above 100 keV) is not expected unless the corona is partially obscured by the precessing disk.

Besides, oscillation of the corona has also been proposed to explain the observed LFQPOs (Cabanac et al. 2010). However, the variations of the corona properties such as the electron temperature predicted by this model was not observed. In addition, an increasing trend of the RMS variability with energy relation predicted by this model is not seen either. Our results rule out the oscillation of the corona as the cause of the LFQPOs.

We have also noticed that the Two-Comptonent Advection Flow (TCAF) is used to explain the X-ray spectral and timing properties of black hole binaries in the hard state. The post-shock region in this model acts as a Compton cloud, and the oscillation of the Compton cloud causes the LFQPO(Chakrabarti et al. 2008). The Keplerian disk is situated outside the shock location and should be very far away from the central black hole (hundreds of r_g) in order to match the observed LFQPO frequency(Debnath et al. 2014). It would be very difficult to produce a strong disk reflection component and the potential oscillation of the Compton cloud further out in such a scenario.

Jet can also act like a corona which produces Compton photons (Markoff et al. 2005). MHD simulations have shown that a precessing jet can be formed and precession of the jet might be responsible for the LFQPO (Liska et al. 2018). Our results are rather consistent with such an idea that the Compton emission from the jet or jet base illuminates the accretion disk and produces the reflection component (e.g. Dauser et al. 2013; Kara et al. 2016). Other proposals which attribute the broadband X-ray LFQPOs as due to processing jet alone (Ma et al. 2020; Ferreira et al. 2022) is not supported by our spectral analysis, as a reflection component with strong effect of reflection fraction is required.

4 CONCLUSION

By performing LFQPO phase-dependent spectral analysis, we found the most varied parameter between the energy spectra corresponding to the peak phase and the trough phase of the black hole LFQPOs is the normalization *norm* in the Comptonization model we applied, and the second most varied parameter is the reflection fraction $\mathcal{R}$. Both the Compton and reflection spectral components contribute to the LFQPOs observed in broadband X-rays. In the spectral model applied in our spectral analysis, the difference in the normalization *norm* represents the variation in the Compton emission component, and the parameter reflection fraction $\mathcal{R}$ serves as an apparent amplification of the incident Compton component into the resulted reflection component, adding additional modulation in the reflection component with the LFQPO phase. Our investigation implies that the original timing signals or beats that are responsible for the LFQPOs lie in the Compton emission component, and the energy-dependent behavior of the LFQPOs at softer energies ($\lesssim 30$ keV) is the result of

the reflection component with a rather large reflection fraction. If the LFQPOs are due to Lense-Thirring precession, the phase information of precession then lies in the Compton component rather than in the reflection component.

DATA AVAILABILITY

The public data used in this work can be downloaded in the *Insight*-HXMT official website (http://hxmten.ihep.ac.cn/)

REFERENCES

Atri P., et al., 2020, Monthly Notices of the Royal Astronomical Society, 493, L81
Belloni T. M., Motta S. E., 2016, arXiv, 440, 61
Buisson D. J. K., et al., 2019, Monthly Notices of the Royal Astronomical Society, 490, 1350
Cabanac C., Henri G., Petrucci P.-O., Malzac J., Ferreira J., Belloni T. M., 2010, Monthly Notices of the Royal Astronomical Society, 404, 738
Casella P., Belloni T., Homan J., Stella L., 2004, Astronomy & Astrophysics, 426, 587
Chakrabarti S. K., Debnath D., Nandi A., Pal P. S., 2008, Astronomy & Astrophysics, 489, L41
Dauser T., Garcia J., Wilms J., Böck M., Brenneman L. W., Falanga M., Fukumura K., Reynolds C. S., 2013, Monthly Notices of the Royal Astronomical Society, 430, 1694
Debnath D., Chakrabarti S. K., Mondal S., 2014, Monthly Notices of the Royal Astronomical Society: Letters, 440, L121
Done C., Gierlinski M., Kubota A., 2007, The Astronomy and Astrophysics Review, 15, 1
Dziełak M. A., Zdziarski A. A., Szanecki M., De Marco B., Niedźwiecki A., Markowitz A., 2019, Monthly Notices of the Royal Astronomical Society, 485, 3845
Esin A. A., McClintock J. E., Narayan R., 1997, The Astrophysical Journal, 489, 865
Fabian A. C., Ross R. R., 2010, Space science reviews, 157, 167
Ferreira J., et al., 2022, Astronomy & Astrophysics, 660, A66
Foreman-Mackey D., Hogg D. W., Lang D., Goodman J., 2013, Publications of the Astronomical Society of the Pacific, 125, 306
Garcia J., Kallman T. R., 2010, The Astrophysical Journal, 718, 695
Huang Y., et al., 2018, The Astrophysical Journal, 866, 122
Ingram A. R., Motta S. E., 2019, New Astronomy Reviews, 85, 101524
Ingram A., van der Klis M., 2015, Monthly Notices of the Royal Astronomical Society, 446, 3516
Ingram A., Done C., Fragile P. C., 2009, Monthly Notices of the Royal Astronomical Society: Letters, 397, L101
Ingram A., van der Klis M., Middleton M., Done C., Altamirano D., Heil L., Uttley P., Axelsson M., 2016, Monthly Notices of the Royal Astronomical Society, 461, 1967
Ingram A., van der Klis M., Middleton M., Altamirano D., Uttley P., 2017, Monthly Notices of the Royal Astronomical Society, 464, 2979
Kara E., Miller J. M., Reynolds C., Dai L., 2016, Nature, 535, 388
Kara E., et al., 2019, Nature, 565, 198

Kawamuro T., et al., 2018, The Astronomer's Telegram, 11399, 1

Liska M., Hesp C., Tchekhovskoy A., Ingram A., van der Klis M., Markoff S., 2018, Monthly Notices of the Royal Astronomical Society: Letters, 474, L81

Ma X., et al., 2020, Nature Astronomy

Mao D.-M., Yu W.-F., Zhang J.-J., Yan Z., Rapisarda S., Wang X.-F., Bai J.-M., 2022, Research in Astronomy and Astrophysics, 22, 045009

Markoff S., Nowak M. A., Wilms J., 2005, The Astrophysical Journal, 635, 1203

Miller J. M., Homan J., 2004, The Astrophysical Journal, 618, L107

Miyamoto S., Kitamoto S., Hayashida K., Egoshi W., 1995, The Astrophysical Journal, 442, L13

Nathan E., et al., 2022, Monthly Notices of the Royal Astronomical Society, 511, 255

Niedzwiecki A., Szanecki M., Zdziarski A. A., 2019, Monthly Notices of the Royal Astronomical Society, 485, 2942

Psaltis D., Belloni T., van der Klis M., 1999, The Astrophysical Journal, 520, 262

Remillard R. A., McClintock J. E., 2006, Annual Review of Astronomy and Astrophysics, 44, 49

Schnittman J. D., Homan J., Miller J. M., 2006, The Astrophysical Journal, 642, 420

Shakura N. I., Sunyaev R. A., 1973, Astronomy and Astrophysics, 24, 337

Shidatsu M., et al., 2018, The Astrophysical Journal, 868, 54

Shidatsu M., Nakahira S., Murata K. L., Adachi R., Kawai N., Ueda Y., Negoro H., 2019, The Astrophysical Journal, 874, 183

Stiele H., Kong A. K. H., 2020, The Astrophysical Journal, 889, 142

Torres M. A. P., Casares J., Jiménez-Ibarra F., Álvarez Hernández A., Muñoz-Darias T., Armas Padilla M., Jonker P. G., Heida M., 2020, The Astrophysical Journal Letters, 893, L37

Tucker M. A., et al., 2018, The Astrophysical Journal Letters, 867, L9

Uttley P., et al., 2018, The Astronomer's Telegram, 1423

van der Klis M., 1995, in X-ray binaries. pp 252–307, https://ui.adsabs.harvard.edu/abs/1995xrbi.nasa..252V

Van der Klis M., 2006, csxs, 39, 39

Verner D. A., Ferland G. J., Korista K. T., Yakovlev D. G., 1996, The Astrophysical Journal, 465, 487

Wilms J., Allen A., McCray R., 2000, The Astrophysical Journal, 542, 914

You B., T. \.Zycki P., Ingram A., Bursa M., Wang W., 2020, The Astrophysical Journal, 897, 27

You B., et al., 2021, Nature Communications, 12, 1025

Yu W., van der Klis M., 2002, The Astrophysical Journal, 567, L67

Yu W., Van Der Klis M., Jonker P. G., 2001, The Astrophysical Journal, 559, L29

Yu W., Lin J., Mao D., Zhang J., Yan Z., Bai J., 2018a, The Astronomer's Telegram, 1591

Yu W., Zhang J., Yan Z., Wang X., Bai J., 2018b, The Astronomer's Telegram, No. 11510, 11510, 1

Zhang S.-N., et al., 2020, Science China Physics, Mechanics & Astronomy, 63, 249502

Zhao X., et al., 2021, The Astrophysical Journal, 916, 108

This paper has been typeset from a TeX/LaTeX file prepared by the author.